



Overlapping regions of coseismic and transient slow slip on the Hawaiian décollement

Jiun-Ting Lin*, Khurram S. Aslam, Amanda M. Thomas, Diego Melgar

Department of Earth Sciences, University of Oregon, 1272 University of Oregon, Eugene, OR 97403, United States of America

ARTICLE INFO

Article history:

Received 29 January 2020
Received in revised form 14 April 2020
Accepted 18 May 2020
Available online 2 June 2020
Editor: M. Ishii

Keywords:

joint inversion
slow slip event
2018 M_w 7.1 Hawaii earthquake
fault mechanics
earthquake cycle modeling
coseismic SSE overlap

ABSTRACT

Earthquakes and slow slip are different faulting processes that release accumulated stress on different time scales. Despite nearly two decades of study, it is still unclear whether the same section of fault is capable of hosting both slow, aseismic and fast, seismic slip. Here, we jointly invert GPS, strong motion records, and empirically corrected tsunami waveforms for the 2018 M_w 7.1 Hawai'i earthquake. Our inversion results suggest the earthquake had a slow rupture speed of 1.2 km/s with a maximum slip of ~ 3 m South-East of the hypocenter extending to the South-West through an area known to regularly host slow slip events. After exploring how the choice of fault geometry and regularization parameters affect the slip distributions of the earthquake and slow slip events we find strong evidence of overlap between the two. Additionally, we perform numerical modeling to simulate fast and slow slip behavior. Due to the homogeneity of the Hawaiian décollement differences in effective stress are likely an important factor that causes the diversity of slip. We find that an earthquake can completely penetrate into the slow slip zone provided the effective stress differences between fast and slow slip zones is large enough to facilitate this. Our results reinforce the idea that an individual section of fault is capable of hosting a variety of distinct slip behaviors. This is important for estimating earthquake rupture extent and for better ground motion and tsunami hazard assessment.

© 2020 Elsevier B.V. All rights reserved.

1. Introduction

1.1. Fast and slow slip

Earthquakes represent rapid release of accumulated strain along faults and typically occur on timescales of fractions of a second to minutes in the largest earthquakes. To generate high frequency seismic waves, typical earthquakes slip at velocities ranging from 10^{-4} to $1+$ m/s (e.g. Galetzka et al., 2015; Thomas et al., 2016). In contrast, slow, transient fault slip occurs on timescales of seconds to years resulting in slip velocities that are usually at most 1–2 orders of magnitude above the plate rate (Bürgmann, 2018). Transient slow slip events were originally discovered down dip of seismogenic zone in Japan and Cascadia (Obara, 2002; Rogers and Dragert, 2003). However, in the nearly 20 years since its original discovery it is now clear that transient slow slip can also occur in the shallow portion of subduction megathrusts (Yamashita et al., 2015; Saffer and Wallace, 2015; Wallace et al., 2016) and within the seismogenic zone (Ito et al., 2013; Dixon et al., 2014).

Regions that regularly host transient slow slip are often observed adjacent to highly coupled regions of subduction megathrusts capable of generating large magnitude earthquakes (e.g. Dixon et al., 2014; Radiguet et al., 2016; Rolandone et al., 2018). This observation naturally raises questions as to whether the same section of fault is capable of hosting both slow and fast slip. If they are, then using only the highly coupled regions of subduction megathrusts to estimate the areal footprint of future earthquakes may fundamentally underestimate rupture extent and earthquake magnitude. Beyond estimating the extent of future earthquakes, the ability of slip to penetrate into regions hosting slow slip has important implications for ground motion and tsunami hazards. For example, in many subduction zone geometries the down dip region of subduction megathrusts is the section of fault closest to major population centers, hence increasing slip in this region will increase ground motions there (Chapman and Melbourne, 2009; Frankel et al., 2015; Ramos and Huang, 2019). In contrast, increasing slip near the trench results in larger sea floor displacements and resulting tsunamis (Satake et al., 2013; Melgar et al., 2016).

Despite the aforementioned implications, to date there is a dearth of observations of regions known to host slow slip overlapping with those that host coseismic slip. Here we show that

* Corresponding author.

E-mail address: jiunting@uoregon.edu (J.-T. Lin).

the 2018 M7.1 Hawaii earthquake (Fig. 1) ruptured the entirety of an adjacent region that regularly hosts transient aseismic slip. After exploring the extent of overlap as a function of fault plane geometry and inversion regularization parameters we find that, for most reasonable choices, the SSEs and coseismic slip overlap nearly entirely with the majority of the SSE regions hosting 1+ m of coseismic slip. Finally, we use simplified numerical models of fault slip to explore the conditions that promote significant overlap and discuss which variations in fault mechanical properties are likely responsible for variations in slip behavior.

1.2. Tectonic setting of Hawaii

The south east flank of Hawaii's Kilauea volcano is a region of complex tectonics that reflect a combination of earthquake and magmatic processes (Owen et al., 1995). Leveling, continuous, and campaign Global Navigation Satellite System (GNSS) measurements indicate that it moves seaward at rates that can exceed 10 cm/yr (Owen et al., 1995; Delaney et al., 1998). This deformation is thought to be driven by unstable gravitational spreading and accumulation of magma along Kilauea eastern rift systems (Thurber and Gripp, 1988) and is accommodated on a décollement dipping shallowly to the NW. The décollement is thought to coincide with the interface between the underlying oceanic crust and the volcanic edifice (Hill, 1969; Furumoto and Kovach, 1979; Nakamura, 1982). As such, the décollement is likely made up of a thin (<1 km) layer of oceanic sediments based on observations of low velocity seismic waves (Thurber et al., 1989) and measurements of sediment thickness in the Pacific basin surrounding Hawaii (Nakamura, 1982). The distribution of seismicity beneath the East rift zone (ERZ) clearly illuminates a planar geometry at a depth of 7~10 km (Klein et al., 1987; Denlinger and Okubo, 1995; Got and Okubo, 2003) that extends seaward, which has been well-constrained by focal mechanisms and seismic reflection data (Gillard et al., 1996; Morgan et al., 2000; Park et al., 2007). Large earthquakes have occurred on the décollement, such as the 1868 M7.9 Kao and the 1975 M_w7.7 Kalapana earthquakes. Additionally, this structure hosts both periodic and aperiodic slow slip events (SSEs).

1.3. Slow slip events in Hawaii

Cervelli et al. (2002) first identified slow slip in GPS data recorded on Kilauea's south flank that manifest as systematic GPS displacements of up to 1.5 cm occurring over a 36 hour period. Those authors found that the displacements were best fit by a shallow, thrust source located at 4.5 km depth. Accounting for material heterogeneity increased the estimated source depth to 5 km which led those authors to conclude that the slow slip was too shallow to be on the décollement. Later, Segall et al. (2006) and Brooks et al. (2006) showed that M5.5-5.9 transient SSEs regularly occur in Hawaii and can be magmatically triggered (Brooks et al., 2008). Additionally, Segall et al. (2006) employed the location and timing of coeval, triggered microseismicity to argue that these SSEs do indeed occur on the décollement. Montgomery-Brown et al. (2009) later showed the accounting for the combined effects of topography and elastic heterogeneity can reconcile the inferred depths of the SSEs with the depths of coeval microseismicity, further supporting the idea that both occur on the décollement.

Additionally, Montgomery-Brown et al. (2009) identified new SSEs with distinct deformation patterns. Foster et al. (2013) later recognized that there are two different asperities that produce SSEs; a western asperity that hosts nearly periodic SSEs that average with typical magnitudes of ~M5.8 and an eastern asperity that hosts irregular ~M5.4 slip events.

2. Methods and results

2.1. The M_w7.1 2018 Hawaii earthquake

The May 4 M_w7.1 Hawaii earthquake is the largest earthquake on the island since the 1975 M7.7 Kalapana earthquake (Owen and Bürgmann, 2006). In addition to widespread strong shaking it produced a tsunami with a maximum wave height of 40 cm recorded at a nearby tide gauge (KAPO, Fig. 1). Different slip models using teleseismic, strong motion, GPS, tsunami data or some combination thereof have been published in the literature (Liu et al., 2018; Bai et al., 2018; Chen et al., 2019). While these models differ in their specifics, their salient features are similar and include peak slip of approximately 3 m on a structure dipping shallowly (5~7.5°) to the NW, with an average rupture speed of approximately 1 km/s. Another common feature of these slip models is they either do not include or fail to completely reproduce near-field tsunami observations at stations HONU and KAPO (Fig. 1). Published inversions for the Hawaii earthquake that have attempted to include the near-field tsunami data ultimately have noted large arrival time discrepancies (e.g. the difference between modeled and observed arrival times as large as ~4 min at KAPO, only 30 km from the hypocenter (Bai et al., 2018)).

Near field tsunami data provide important constraints on rupture extent and total moment (Satake et al., 2013), hence reproducing these observations is important because the 2018 Hawaii earthquake occurred almost completely offshore. We note that large tsunami misfits may indicate that flank failure may have occurred as part of the 2018 event, similar to the 1975 Kalapana earthquake discussed by Owen and Bürgmann (2006). However, our analysis completely rules out this possibility. Careful examination of the tide gauge records reveals a small tsunami signal resulting from a M_w5.7 foreshock which occurred ~1 hr before the mainshock with very similar source location and focal mechanism (Fig. 2). This small event also has a significant time delay. This timing issue in near-field recordings has been noted before (Romano et al., 2016) and is attributed to artificial delays introduced into modeling of the tsunami propagation by the finite resolution of the digital bathymetric model in the near-shore region where tide gauges are located. To correct for this issue, we employ a novel empirical time calibration technique to the tsunami data recorded at near-field stations. We take the tsunami from M_w5.7 foreshock recorded at both tide gauges and use it to find the optimal time shift for the M_w7.1 mainshock tsunami record. The tsunami waveforms of the M_w5.7 foreshock and mainshock are very similar as they share nearly identical path and site effects. Because the M_w5.7 earthquake is a relatively small event, it can be treated as a point source. We use the W-phase moment tensor solution to calculate the expected coseismic seafloor deformation and use this as the tsunami initial condition. We model its propagation model to both tide gauges and obtain the timing misfit by cross correlation between the modeled and observed arrivals. The time shifts between synthetic and observations are 240 s and 135 s for KAPO and HONU, respectively. These delays are employed as empirical time corrections for the mainshock inversion and lead to good fits to the data.

We determine the slip distribution of the 2018 earthquake by jointly inverting the time-corrected tide gauge data, GPS measurements of permanent deformation (static offsets), and strong motion records. Data fits are shown in (Fig. S1). The resulting slip model explains the near-field tsunami observations, suggesting that no slope failure process was involved in the 2018 event. We provide details on the inversion method in the supplementary material. In our preferred model, slip occurs on an asperity located southeast of the hypocenter (Fig. 1) with a maximum slip of 3.2 m at a depth of 3.5 km resulting in an overall M_w7.1 event.

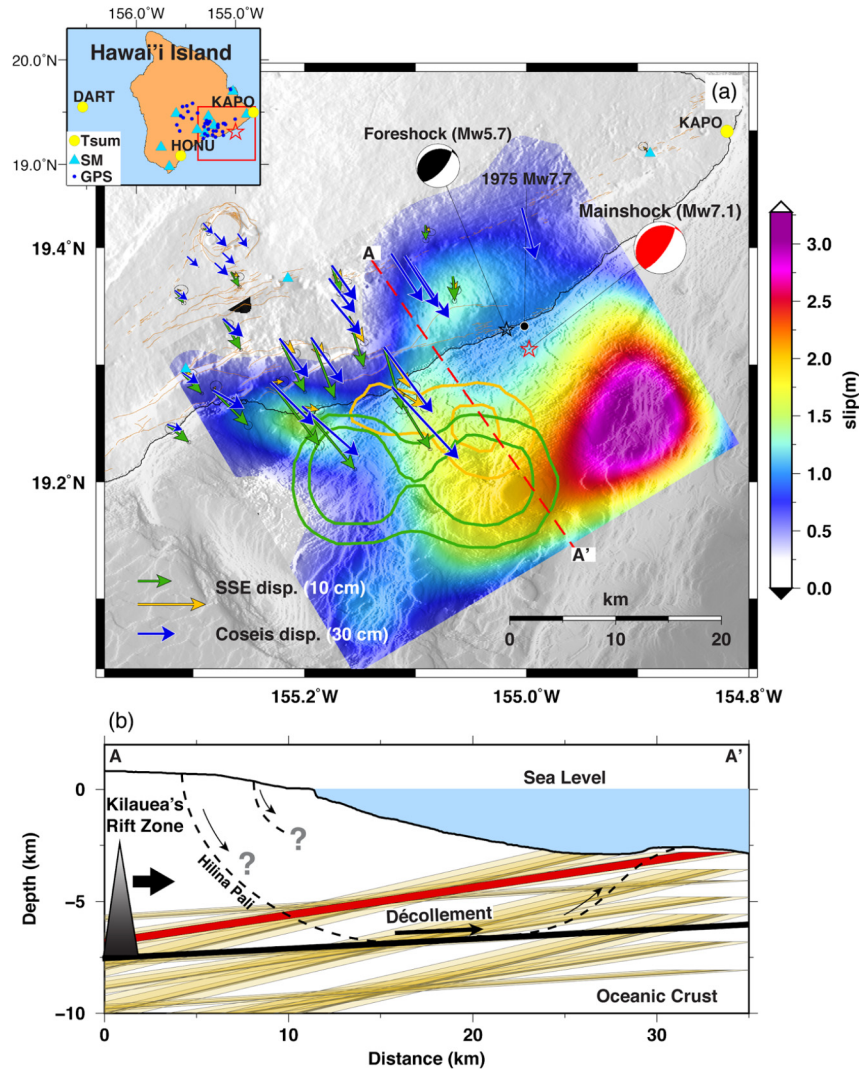


Fig. 1. Map of southeastern Hawai'i island. (a) Blue, orange and green vectors show the recorded GNSS horizontal displacements from the 2018 M_w 7.1 earthquake, SSE-East and SSE-West, respectively. Triangles denote the strong motion stations from the Hawaiian Volcano Observatory network. The yellow circles represent tide gauges (KAPO, HONU) and one DART buoy (DART). The colormap shows the joint GPS, strong motion and corrected tsunami inversion for the 2018 earthquake on the same fault plane of Liu et al. (2018). Orange and green contours mark the SSE areas of Foster et al. (2013). Focal mechanisms and hypocenters (stars) are taken from the USGS NEIC, including the M_w 5.7 foreshock (20180504T21:32:44) shown in black and the mainshock (red). Brown lines denote regional active faults identified by the USGS. (b) Cross section along the red line shown in Panel A (a). The black triangle indicates the Kilauea's eastern rift system. Black lines represent the décollement of Hawaiian flank and the oceanic crust inferred by Morgan et al. (2000) (reflection profile 2 in Fig. 4) and the structures modified from Montgomery-Brown et al. (2009, Figure 18). Brown rectangles show all 45 fault geometries (i.e. projected from 3D to 2D) explored in our overlap analysis described below (shown in Fig. 3a). The red rectangle marks the fault of Liu et al. (2018) that is also shown in Fig. 1(a). (For interpretation of the colors in the figure(s), the reader is referred to the web version of this article.)

Our preferred slip pattern also shows that the 2018 event ruptured southwest of the hypocenter toward the SSE area. We find a preferred rupture velocity of 1.2 km/s (Fig. S2), consistent with the results of previous studies (Liu et al., 2018; Bai et al., 2018). Considering the 3.7 km/s shear wave velocity at this depth (Table S1), this is a relatively slow rupture speed. Analysis of rupture progression indicates the rupture front reached the main asperity 10s after initiation, gradually ruptured to the southwest beginning at 17s, and ceased after 32s (Fig. S3). We also test the joint inversion with corrected and uncorrected tsunami waveforms, and the result shows that the model cannot explain tsunami data without empirical time corrections (Fig. S4).

Although the fault geometries of the 2018 earthquake employed in previous studies (e.g. Liu et al., 2018; Bai et al., 2018; Chen et al., 2019) seem to be distinct from the décollement, i.e. they have a shallower preferred depth of ~ 6 km and a steeper fault dip of $\sim 7^\circ$ or 20° according to the USGS W-phase moment tensor, this possibility has been ruled out by Chen et al. (2019). As they show,

the fault depth is not very sensitive to the data they used in their joint inversion (i.e. teleseismic, GPS and strong motion) since the variance reduction (VR) only changes by up to 2% when varying the hypocentral depth between 5 and 9 km. Thus, the preferred shallower fault plane is only a plausible solution and we can only resolve the geometry within some range based on reasonable constraints (Table 1) from grid-searching, not a global minimum of the models. Also, the initial dip angle of 20° from USGS was refined by a later analysis of Love Wave radiation patterns to between 2.5 – 7.5° (Lay et al., 2018), suggesting the 2018 earthquake took place on a fault plane with a geometry similar to the décollement.

2.2. Overlap of slow and fast slip

The results presented above suggest that there is significant overlap between the 2018 earthquake and SSE slip distributions so we now explore to what extent coseismic slip overlaps with SSEs. The relatively simple faulting environment and very dense modern geophysical observations when compared to subduction zone set-

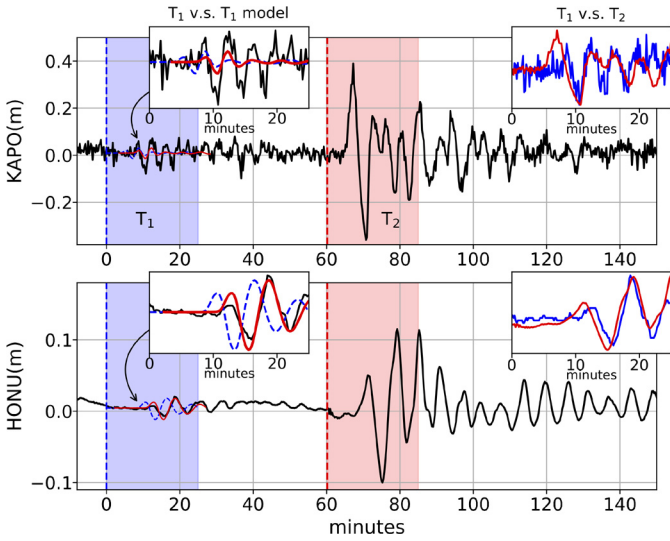


Fig. 2. Tsunami waveforms and empirical tsunami correction. The blue (T1) and red (T2) areas mark the tsunami data from foreshock and mainshock, respectively. Inset T1 v.s. T1 model shows the tsunami model (blue dashed line) and the shifted model (red line) of the foreshock. The shifts are then used to correct the unmodeled error in the mainshock tsunami. Inset T1 v.s. T2 shows the normalized tsunami of foreshock (blue) and mainshock (red).

Table 1
Constraints for the grid-searched inversions.

	Earthquake	SSE-West	SSE-East
M_w	$6.9 < M_w < 7.3$	$5.5 < M_w < 6.1$	$5.2 < M_w < 5.6$
VR_{GPS}	$VR > 70$	$VR > 80$	$VR > 50$
$Slip_{max}(m)$	$1 < Slip_{max} < 5$	$0 < Slip_{max} < 1$	$0 < Slip_{max} < 0.8$

tings (e.g. Yamashita et al., 2015; Wallace et al., 2016; Ito et al., 2013; Dixon et al., 2014) make Hawaii Island an ideal place to explore this question. Owing to the large magnitude and associated fault dimension (i.e. >30 km), all studies of the 2018 earthquake agree the event, like the SSEs, ruptured the décollement (Liu et al., 2018; Bai et al., 2018; Chen et al., 2019). In order to determine the extent of overlap, we re-invert GPS data from Foster et al. (2013) for the SSE slip distribution; and jointly invert GPS, strong motion, and tsunami records for the earthquake slip distribution using the same inversion method introduced in the supplementary material. Our checkerboard tests show good resolution for the earthquake inversion, and satisfactory resolution in the SSE source region (Fig. S5). Because of the uncertainties in both the location and geometry of the décollement, we test a range of fault geometries with strikes of 229° – 249° , dips of 3° – 11° , and depth of 5–9 km; a total of 45 possible fault geometries. We also grid search Laplacian spatial regularization for each geometry. Rather than determining a best fit fault plane and slips we consider all possible models that have a reasonable VR and moment magnitude when compared to far-field moment tensor solutions and results from different sources of joint inversion (Bai et al., 2018; Liu et al., 2018; Chen et al., 2019), defined in Table 1. Note that for SSEs, only the VRGPS is considered. For the earthquake, the joint inversion has regularized all the dataset together and VRGPS above 70 should give satisfactory models that will be used for our overlap analysis discussed below. Detailed calculations are provided in the supplementary material.

We define overlap as the area between the contours corresponding to 50% of the peak SSE and earthquake slip from our inversions. We note that top 50% of slip is a strict criterion, however, our goal is to qualitatively check whether the slip distributions overlap, and not to determine the exact overlapping area. Therefore, a strict threshold slip criterion avoids contributions from small localized slip patches that result from underregularization.

Fig. 3 summarizes the overlap measurements for earthquake and the two SSE families. Slip inversion results for all 45 fault geometries are shown in Fig. S7. In Fig. 3a, panels on the left and right represent the western and eastern SSE respectively. Each row represents a different centroid depth of 5, 7, and 9 km. The size of gray circles in Fig. 3a shows the overlapping areas of all the possible earthquake and SSEs models that fit the criteria in Table 1 for the associated strike and dip. We note that due to a wide range of regularization parameters, there may be multiple inversion results that satisfy the criteria in Table 1 for any given geometry. Thus, we average all the possible models since the most appropriate model is the one that shares common features that are emphasized by averaging (color coded circles in Fig. 3a). We also note that there are some models that rupture to the edge of the fault plane (e.g. Fig. 3c, 3d), which are end-members that satisfy the criteria in Table 1, and are downweighted by averaging. Our results indicate that when the fault moves closer to the décollement dip of 3° , the average overlap systematically increases for both families. This supports the idea that significant overlap must occur for most reasonable choices of fault geometry if the SSEs and coseismic slip occur on the same fault plane. The tests show that the overlap is not sensitive to depth of 5 and 7 km. This is likely because the insensitivity of inversion for depth, consistent to the test of Chen et al. (2019). However, for the centroid depth of 9 km, the model does not favor the steep geometry, which extends the fault to 12 km depth. This depth is below the décollement (Fig. 1b) and only a few models can pass our constraints, making small to no overlap for most of the slip inversions (Fig. 3a).

2.3. Modeling slip penetration

The physical mechanism that gives rise to slow fault slip and that best represents the range of natural slow-slip phenomena is still debated. Producing events that slip slowly requires that slip be able to nucleate and accelerate but quench at moderate slip speeds. Numerical models that reproduce this behavior have i) incorporated frictional rheologies that change from rate weakening to rate strengthening at a threshold slip rate (e.g., Hawthorne and Rubin, 2013), ii) included mixtures of rate-weakening and rate-strengthening (Skarbek et al., 2012) or viscous materials (e.g., Ando et al., 2012), iii) called upon dilatancy to stabilize slow rupture (e.g., Segall et al., 2010) and iv) appealed to a characteristic length scale to stabilize rupture (Liu and Rice, 2009; Rubin, 2008).

Rate and state friction characterizes the frictional behavior of faults observed during laboratory experiments (Dieterich, 1978, 1979; Ruina, 1983) and casts the friction coefficient as a function of slip rate and a single state variable (Dieterich, 1979; Ruina, 1983). Here, we model the fault strength τ using a form of the rate and state friction law given by

$$\tau(V, \theta) = f_0 \sigma + a \sigma \log \left(\frac{V}{V_0} \right) + b \sigma \log \left(\frac{V_c \theta}{D_c} + 1 \right), \quad (1)$$

where σ is the effective normal stress, a and b are dimensionless material constants, V is the slip rate, θ is the state variable which evolves according to slip law (supplementary material), D_c is the critical slip distance over which the state variable evolves, V_c is the cut off velocity (e.g. Hawthorne and Rubin, 2013), and V_0 and f_0 are reference values of slip rate and friction, respectively.

To explore the conditions that give rise to the observed overlap between slow slip and co-seismic regions, we employ a boundary element model of a 1D fault embedded within a 2D whole space (see supplementary material for details). This 1D fault (Fig. 4a) corresponds to along-strike length of the fault at a fixed seismogenic depth. The values of all the parameters used in this study are provided in Table S2. We model both the coseismic zone (CSZ) and

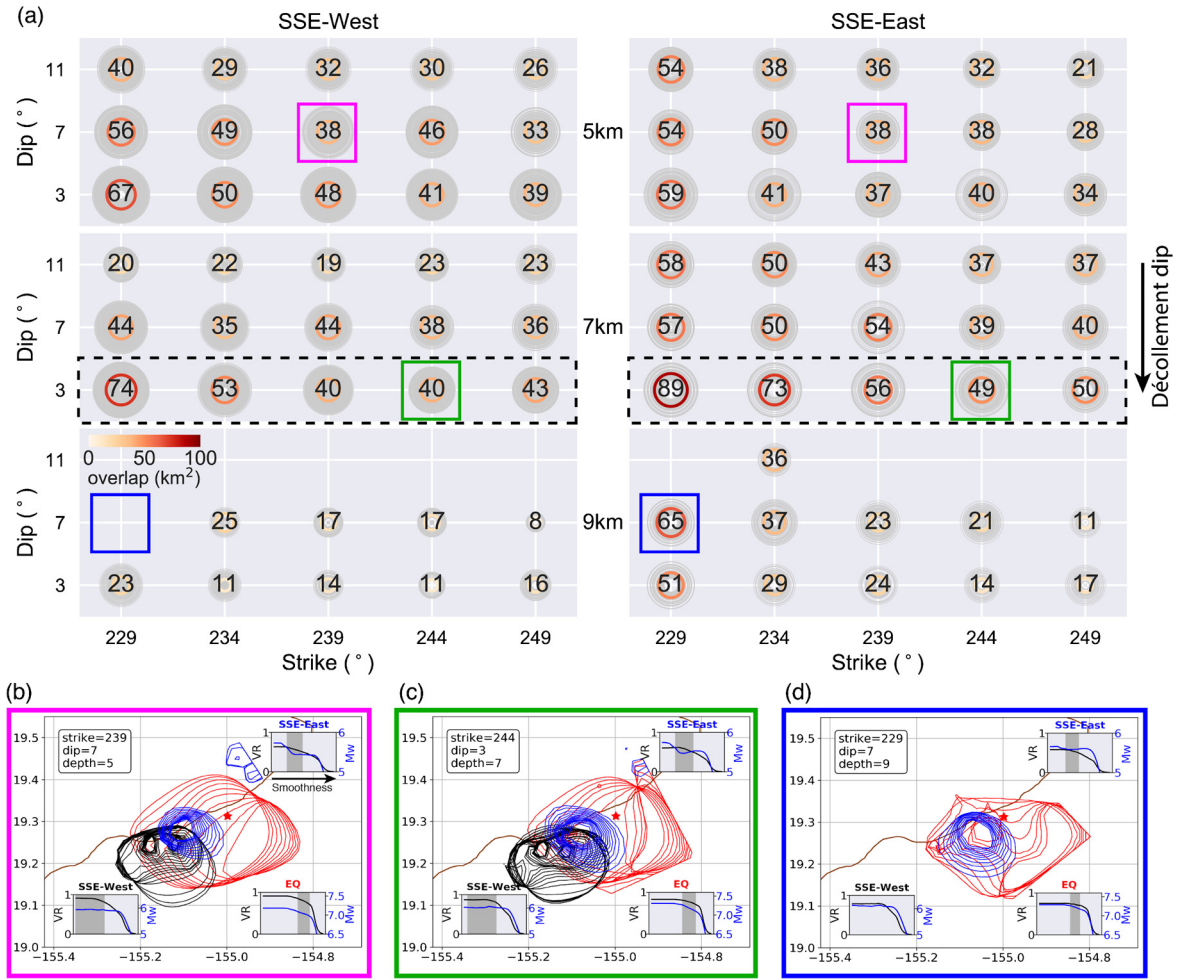


Fig. 3. Overlapping areas of coseismic slip and SSEs from our inversion tests. **(a)** The light gray circles show the overlapping areas of all the possible solutions. Colored circles show the averaged of the light gray circles with numbers denoting the averaged overlapping area (in km²). Dashed black boxes mark the preferred décollement dip and depth. **(b)–(d)** show examples of overlapping calculations with (229°, 7°, 5 km), (244°, 3°, 7 km) and (229°, 7°, 9 km) for strike dip and depth, respectively. The red, blue and black lines mark the top 50% of slip from the earthquake, East SSE and West SSE inversion, respectively. Gray areas in the insets show the solutions that fit the given VR, M_w and maximum slip constraints (Table 1).

slow slip zone (SSZ) using rate-weakening properties and values of V_c that are above and below coseismic slip rates respectively. We chose a velocity weakening-to-strengthening rheology because it is relatively simple to implement and will allow us to gain insight into the first-order interactions between slow and fast slip. Our intent is not to endorse Eq. (1) as the definitive rheology responsible for slow earthquakes. Similarly, our goal here is not to reproduce the exact characteristics of the SSEs and earthquakes on the décollement, but rather to build a model that reproduces some of the characteristics of that system in order to gain insight into which conditions promote coseismic slip penetrating into a region favorable for hosting SSEs.

In the model, we prescribe $V_c \ll$ co-seismic slip rates within the SSZ to reproduce slow slip behavior, while the value of V_c is of the order of co-seismic slip rates within the CSZ. It is important to note that a model that reproduces the long recurrence interval co-seismic patch juxtaposed with a comparatively shorter recurrence interval slow slip patch requires further contrast of a , b , D_c , or σ values between the SSZ and the CSZ. We do not expect major changes in temperature between the CSZ and the SSZ as the CSZ to SSZ transition occurs along the fault strike. Additionally, as the décollement is lithologically homogenous (Nakamura, 1982), we do not expect large variations in a , b , or D_c . As such, the difference between effective stress of the SSZ and the CSZ may play an important role in controlling the contrasting slip behavior of the SSZ

and the CSZ. This contrast is well motivated owing to the abundance of observations suggesting that globally regions that host transient slow slip operate at very low effective stress (e.g. Thomas et al., 2012). In our models, we primarily focus on how varying the effective stress affects coseismic rupture propagation and its penetration into the SSZ. We prescribe $\sigma^{SSZ} < \sigma^{CSZ}$ for most of our simulations. However, a few simulations are also performed using $\sigma^{CSZ} = \sigma^{SSZ}$; in this case we assume $D_c^{SSZ} < D_c^{CSZ}$ to explore the effect of similar effective stresses on coseismic rupture.

Fig. 4(b) shows the time evolution of the slip rate within the SSZ and the CSZ for the case of $D_c^{SSZ} < D_c^{CSZ}$ for $D_c^{SSZ} = 4$ mm, the $D_c^{CSZ} = 20$ mm, $\sigma^{CSZ} = 10$ MPa, and $\sigma^{CSZ} = \sigma^{SSZ}$. Fig. 4(b) shows that this model successfully reproduces earthquake cycles on both the CSZ and the SSZ. Additionally, coseismic events (CSEs, Fig. 4(c)) have longer recurrence intervals and many SSEs nucleate within the SSZ during the interseismic period. Fig. 4(d) and Fig. 4(e) show slip evolution at individual grid points within the CSZ and SSZ respectively. When a SSE nucleates, it mainly stays within the SSZ with either no or very slight penetration into the CSZ. This slight penetration of SSEs generally happens late in the earthquake cycle for the models we explored (Fig. 4(b)). Segall and Bradley (2012) observed similar SSE penetration prior to the onset of a megathrust earthquake in their 2D depth-dependent model. When coseismic rupture starts, it penetrates into the SSZ, but the total penetration of the rupture into the SSZ varies (Fig. 5 and 6). The penetration of

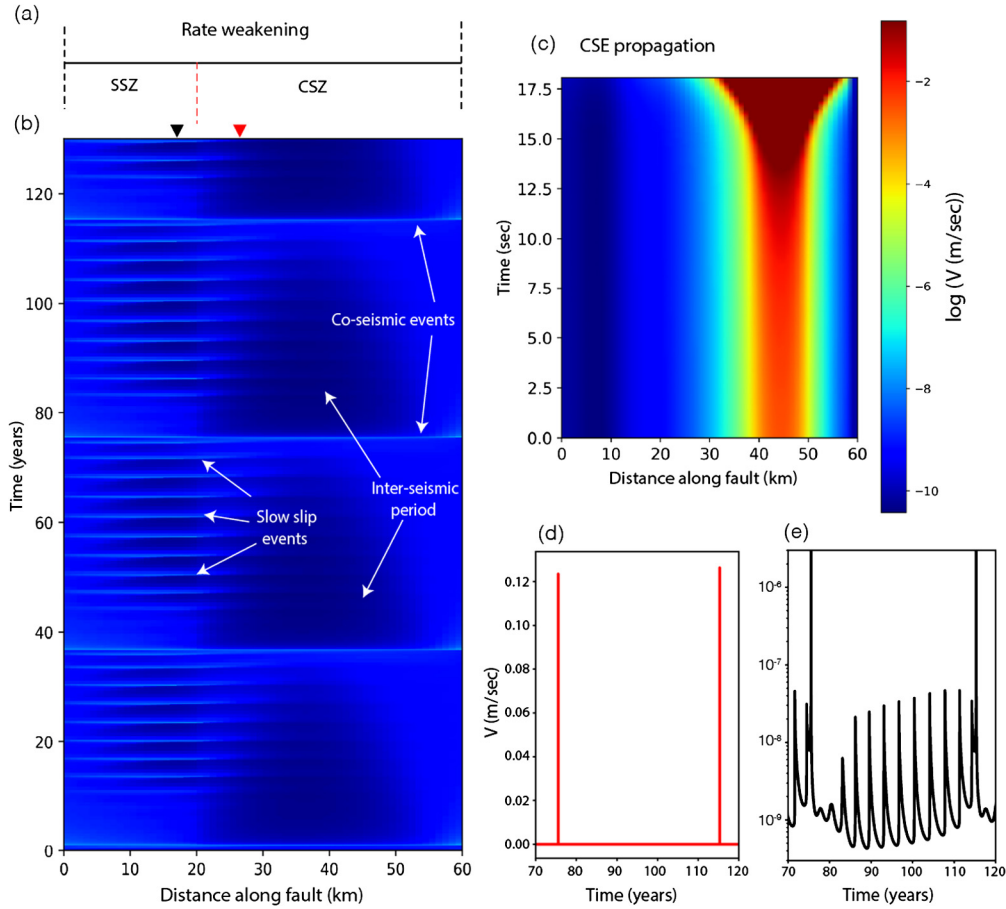


Fig. 4. Model setup and time evolution of slip rate within the slow slip zone (SSZ) and the co-seismic zone (CSZ). **(a)** Model setup of our simulations. We model the fault with rate weakening properties. The fault is divided into two parts. First 20 km of the fault represent the SSZ, while last 40 km of the fault represent the CSZ. The value of V_c is different for both the CSZ and the SSZ ($V_c^{SSZ} < V_c^{CSZ}$). **(b)** The slip rate evolution along the whole length of the fault. The value of σ^{CSZ} and σ^{SSZ} is kept the same (10 MPa), while D_c^{SSZ} value is 20 mm, and the D_c^{CSZ} value is 4 mm. We observe many slow slip events (SSEs) nucleating within the SSZ between two co-seismic events (CSEs). Both the SSEs and CSEs are labeled. **(c)** The initiation and propagation of the CSE within the CSZ. As the rupture expands from its initial location, the slip rate increases and rupture grows. A complete CSE rupture is shown in Fig. 5. **(d)** Slip rate evolution for a single grid point within the CSZ (red triangle in Fig. 4(b)) covering two CSEs. **(e)** Slip rate evolution for a single grid point within the SSZ (black triangle in Fig. 4(b)) covering two CSEs. The penetration of CSE into the SSZ results in a shorter recurrence of SSE right before a CSE. The colorscale is the same for both b and c.

a CSE into the SSZ can be observed in Fig. 4(e), where the recurrence interval of SSEs shortens due to coseismic slip.

To investigate co-seismic rupture penetration from the CSZ to the SSZ, we select three different levels of σ^{CSZ} and seven different values of the effective stress ratio ($\sigma^{SSZ}/\sigma^{CSZ}$) to explore the influence of effective stress on CSE propagation characteristics. Fig. 5 (a-c) show three different example rupture scenarios involving rupture penetration from the CSZ to the SSZ during a CSE. The first rupture scenario typically occurs at higher effective stress ratios (> 0.6), and is shown in Fig. 5(a). A rupture nucleates within the CSZ (Fig. 5(a), blue curves), and then expands within CSZ (green curves). The propagation speed with which the rupture expands is observed to vary in each simulation. Rupture begins decelerating at the CSZ-SSZ interface as it penetrates into the SSZ. The rupture deceleration is marked in Fig. 5(a). During penetration of the rupture into the SSZ, no secondary nucleating patch within the SSZ is observed, and thus the rupture can be considered as a single rupture, penetrating from the CSZ to the SSZ. The second rupture scenario occurs at an intermediate effective stress ratio (0.6-0.4), and is shown in Fig. 5(b). Rupture nucleates and expands within the CSZ (Fig. 5(b), blue and green curves). Once it hits the CSZ-SSZ interface, a small secondary patch within the SSZ nucleates. The secondary patch is labeled in Fig. 5(b). This secondary patch nucleation results in the larger penetration of the rupture as compared to the first case. The final rupture scenario occurs at

a lower effective stress ratio and is shown in Fig. 5(c). A primary rupture nucleates within the CSZ, while before the co-seismic rupture hits the CSZ-SSZ interface, we observe nucleation occurring on a secondary patch within the SSZ. Both the primary and secondary nucleation can be observed in Fig. 5(c). Since the effective stress is significantly lower within the SSZ, the elastic stress changes from the primary slip patch assist in the nucleation of the secondary pulse. Once the rupture front from the CSZ reaches the CSZ-SSZ interface, the pre-existing secondary rupture facilitates rupture into the SSZ, which in most of our simulations results in a 100% penetration (or complete penetration) of the CSE into the SSZ.

Fig. 6(a) and Fig. 6(b) shows the percent penetration of coseismic rupture into the SSZ for different σ^{CSZ} levels and different values of the effective stress ratio. The percent penetration is defined as the ratio of the length of the SSZ ruptured by the CSE to the total length of the SSZ. Fig. 6(a) shows penetration of a CSE for $V_c^{SSZ} = 10^{-8}$ m/s, while Fig. 6(b) shows penetration of CSE for $V_c^{SSZ} = 10^{-6}$ m/s respectively. The minimum CSE penetration is observed to be 37% in Fig. 6(a) and 48% in Fig. 6(b). Minimum penetration occurs at high σ^{CSZ} ($= 10$ MPa), and a high effective stress ratio ($= 0.8$). For σ^{CSZ} values of 5 MPa and 2.5 MPa (shown in Fig. 6(a), and 6(b) by triangles, and circles respectively), we observe lesser rupture penetration for higher effective stress ratios, comparatively more rupture penetration for smaller stress ratios, while complete rupture penetration occurs at the smallest stress

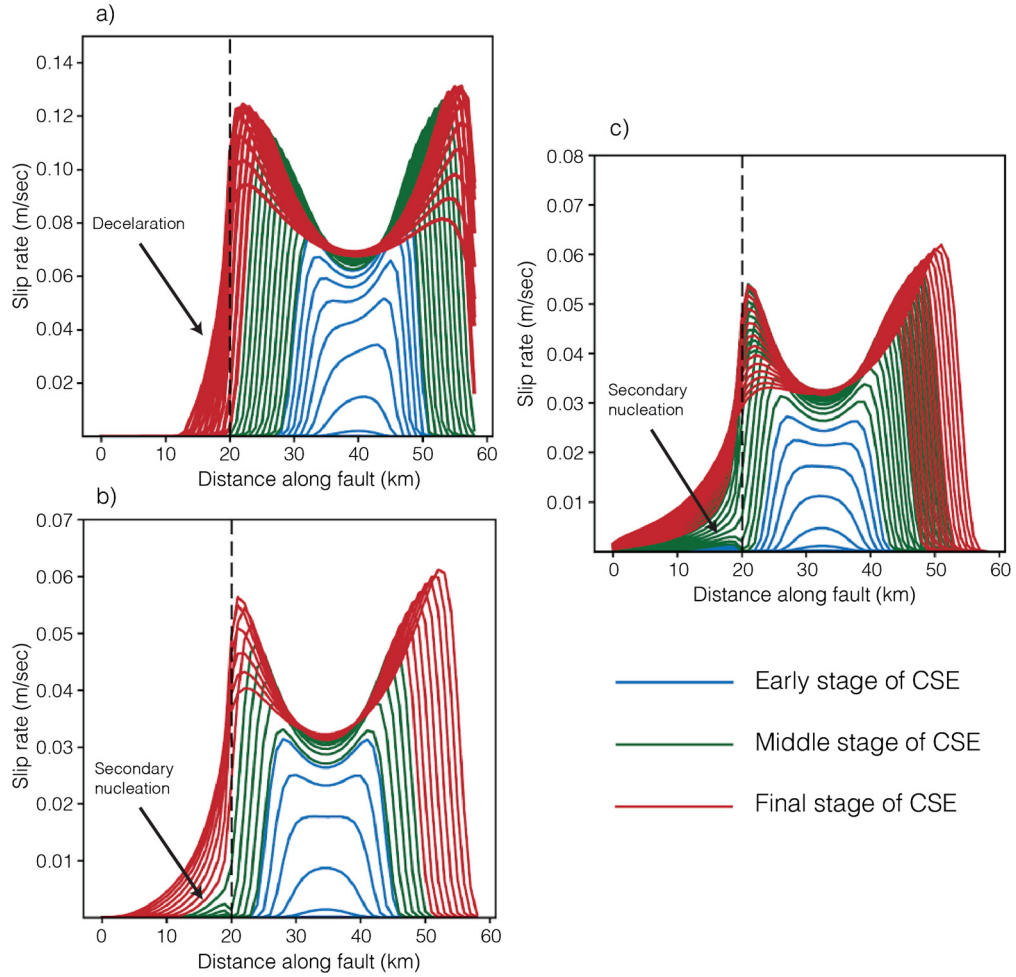


Fig. 5. Different CSE rupture scenarios observed in this study. Each curve represents a time snapshot of slip rate as a function of distance along fault, not equally spaced in time. Note that the time step decreases as the slip speed increases. Different colors represent different stages of the CSE rupture. The blue color represents the early stage of a CSE. This is the stage when rupture initiation occurs. The green color shows the middle stage of a CSE. This is the stage when the rupture grows and expands along the fault, reaches the CSZ-SSZ interface. The red color shows the final stage of a CSE, this stage marks the onset of the rupture termination. (a) The first CSE rupture scenario (with stress ratio = 0.7, $\sigma^{CSZ} = 10$ MPa) where no secondary nucleating patch within the SSZ is observed. (b) The second rupture scenario (with stress ratio = 0.4, $\sigma^{CSZ} = 5$ MPa) where a small secondary patch within the SSZ nucleates when the primary rupture reaches the CSZ-SSZ interface. (c) The third rupture scenario (with stress ratio = 0.2, $\sigma^{CSZ} = 5$ MPa) where a secondary patch nucleation is observed before the primary rupture reaches the CSZ-SSZ interface.

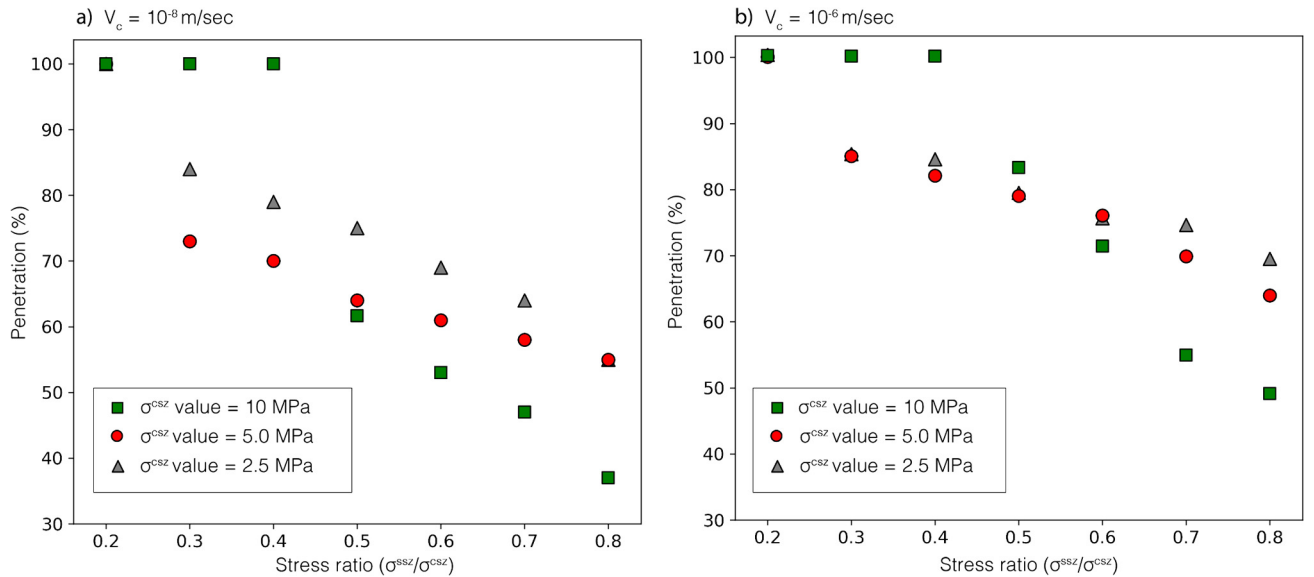


Fig. 6. The percentage penetration of CSE into the SSZ for different σ^{CSZ} and stress ratios ($\sigma^{SSZ}/\sigma^{CSZ}$). (a) Shows the percentage penetration of CSE into the SSZ when $V_c^{SSZ} = 10^{-8}$ m/s. (b) same as (a), but when $V_c^{SSZ} = 10^{-6}$ m/s.

ratio used in this study. For a σ^{CSZ} value of 10 MPa (shown as squares in Fig. 6(a), and 6(b)), we observe lesser rupture penetration for higher stress ratios (similar to smaller σ^{CSZ} levels), but complete rupture penetration occurs at relatively higher stress ratio as compared to smaller stress levels. The complete rupture penetration at high σ^{CSZ} (indicated in Fig. 6(a) and Fig. 6(b) by squares at 100% penetration levels for stress ratios of 0.2, 0.3 and 0.4) suggest that larger stress drops may drive a complete rupture penetration at comparatively larger stress ratios as compared to smaller stress drops. Note that the D_c values are same for different cases presented in Fig. 6, and hence results from Fig. 6(a) and 6(b) suggest that the rupture penetration mainly depends on the stress ratio, and a complete CSE penetration (into the SSZ) can occur under favorable stress conditions. This further suggests that the rupture penetration within the SSZ is largely assisted by the secondary pulse nucleation that helps the rupture to move farther within the SSZ. The overall behavior of the rupture penetration as a function of stress ratio remains the same for the different V_c^{SSZ} values used in this study (Fig. 6(a) and 6(b)) i.e. a larger rupture penetration occurs for smaller stress ratios, while comparatively lesser rupture penetration occurs at higher stress ratios. Additionally, we observe that higher V_c^{SSZ} values result in larger rupture penetrations for similar σ^{CSZ} and stress ratios. Finally, we also calculate the average rupture speeds of different CSE ruptures shown in Fig. 6 and Fig. S6 by dividing the total distance covered by a CSE along the fault by the total time taken by that CSE rupture. Although these calculated rupture speeds are not exact (due to quasi-dynamic approximation used here), these do not appear to be a significant factor in controlling the percent penetration i.e. a slower coseismic rupture may result in complete SSZ penetration under favorable stress conditions.

3. Discussion

Our analysis presented above clearly documents that the slip distribution of the 2018 M7.1 Hawaii earthquake overlaps with the slip distributions of regularly occurring slow slip events. As mentioned in the introduction, overlapping regions of slow and coseismic slip have been either observed or inferred by previous authors (Ito et al., 2013; Tsang et al., 2015; Clark et al., 2019). However, these studies are either not based on modern geodetic data, do not thoroughly explore inversion parameters, or do not explore the overlap in detail. For example, Ito et al. (2013) solved for a fault on subduction zone interface with assuming homogeneous slip to fit ocean-bottom pressure gauge data. The inversion results we show here explore the role of fault geometry and regularization constraints on the resulting coseismic and slow slip distributions and summarize the reasonable models. Additionally, the checkerboard test demonstrates that our joint inversion for earthquake is robust, and has overall good resolution (Fig. S5). We note that the inversion for SSEs has low resolution in up-dip area far offshore. However, since most of the overlapping slip regions occur where both the earthquake and SSEs have good resolution (i.e. mid-Western fault plane), we contend that it is a robust feature, and the 2018 Hawai'i earthquake ruptured a significant fraction of the region that regularly hosts slow slip events.

One limitation of the inversion practices we employed is that they have limited spatial resolution and hence we cannot, through inversion alone, rule out the possibility that the SSEs and coseismic slip occurred on nearly parallel fault planes closely separated in depth. However, we consider this unlikely. Rupture of a shallower high angle splay (Fig. 1b) is a possibility, but owing to its large spatial extent (width usually >30 km), all studies of the 2018 earthquake argue or assume that it ruptured the low-angle décollement (Liu et al., 2018; Bai et al., 2018; Chen et al., 2019). While the locations of the SSEs were also originally unclear, the

work of Segall et al. (2006) and Montgomery-Brown et al. (2009) demonstrate that they too coincide with and are likely hosted by the décollement. In addition to the results we present here, a previous study that employed detailed trilateration measurements has shown that the 1975 Kalapana earthquake ruptured predominantly to the South-West of its hypocenter (Owen and Bürgmann, 2006). If the same region hosting SSEs today is persistent and existed in 1975, then this rupture likely completely ruptured the SSE area, providing another piece of evidence for overlapping regions of slow and fast slip.

While the specific mechanism that gives rise to slow, transient fault slip is still not known, that mechanism must allow for slip events that accelerate to slip rates 1-2 orders of magnitude higher than the background loading rates but not favor further increases in slip rate. Despite this, our observations indicate that it is possible to have coseismic rupture in regions that regularly host slow slip. Our model setup is motivated by geologic interpretations of the Hawaiian décollement and observed along-strike variation between coseismic and slow slip zones implying that frictional properties and other material properties should be relatively homogenous. Our simulation results suggest that lower effective stress ratios, i.e. larger contrasts between effective stress between the SSZ and the CSZ, promote penetration of the CSE into the SSZ resulting in larger overlap. Additionally, the effective stresses within the SSZ and the elastic stress changes from the primary slip patch (within the CSZ) control the overlap characteristics of the CSZ-SSZ such that even coseismic ruptures with slower overall rupture velocities, as observed in the 2018 Hawaii earthquake, can easily rupture the adjacent SSZ. While more realistic transitions in effective stress between the CSZ and SSZ would undoubtedly influence our estimates of penetration, the general result that coseismic rupture is capable of rupturing well into regions hosting slow slip is also supported by the modeling results of Ramos and Huang (2019).

4. Conclusions

We provide strong evidence of overlapping fast and slow slip on the Hawaiian décollement. Joint inversion of GPS, strong motion and tide gauge tsunami observations clearly reveals the slip pattern of the 2018 M_w7.1 Hawai'i earthquake. After thoroughly exploring inversion parameters we find that the earthquake likely ruptured an adjacent region regularly hosts transient slow slip events. Furthermore, we performed quasi-dynamic modeling in 2D with rate and state friction to simulate how coseismic ruptures interact with adjacent regions that host slow slip. The unique tectonic setting of the Hawaiian décollement suggests differences in effective stress are likely a key control on slip diversity. Our modeling results suggest that fast slip can easily penetrate into the slow slip zone, as we observe. Our result reinforces the idea that an individual section of fault is capable of hosting a variety of distinct slip behaviors, and provides observational and theoretical evidence that a fault undergoes slow slip behavior can also rupture seismically. This behavior may also be a common feature in other tectonic environments such as subduction zones. As such, earthquake magnitude forecasts should include adjacent slow slip regions in estimates of areal extent and magnitude.

Declaration of competing interest

The authors declare that they have no known competing financial interests or personal relationships that could have appeared to influence the work reported in this paper.

Acknowledgement

We would like to thank editor Dr. Miaki Ishii and two anonymous reviewers for their valuable feedback. Seismic data we use in this study were downloaded from the Incorporated Research Institutions for Seismology data management center (IRIS DMC). GPS data were accessed through Nevada Geodetic Laboratory (<http://geodesy.unr.edu/>). We thank Victor Sardina at the Pacific Tsunami Warning Center for access to the tide gauge data. We also thank James Foster for sharing the GPS data used in his original slow slip inversions. We thank the Research Advanced Computing Services, University of Oregon for the computing resources. Financial support for this study was provided by National Aeronautics and Space Administration NSSF grant 80NSSC18K1420 and National Science Foundation Award #1663834.

Appendix A. Supplementary material

Supplementary material related to this article can be found online at <https://doi.org/10.1016/j.epsl.2020.116353>.

References

- Ando, R., Takeda, N., Yamashita, T., 2012. Propagation dynamics of seismic and aseismic slip governed by fault heterogeneity and Newtonian rheology. *J. Geophys. Res., Solid Earth* 117 (B11).
- Bai, Y., Ye, L., Yamazaki, Y., Lay, T., Cheung, K., 2018. The 4 May 2018 Mw 6.9 Hawaii island earthquake and implications for tsunami hazards. *Geophys. Res. Lett.* 45 (20), 11–040.
- Brooks, B.A., Foster, J.H., Bevis, M., Frazer, L.N., Wolfe, C.J., Behn, M., 2006. Periodic slow earthquakes on the flank of Kilauea volcano, Hawaii. *Earth Planet. Sci. Lett.* 246 (3–4), 207–216.
- Brooks, B.A., Foster, J., Sandwell, D., Wolfe, C.J., Okubo, P., Poland, M., Myer, D., 2008. Magmatically triggered slow slip at Kilauea Volcano, Hawaii. *Science* 321 (5893), 1177.
- Bürgmann, R., 2018. The geophysics, geology and mechanics of slow fault slip. *Earth Planet. Sci. Lett.* 495, 112–134.
- Cervelli, P., Segall, P., Johnson, K., Lisowski, M., Miklius, A., 2002. Sudden aseismic fault slip on the south flank of Kilauea volcano. *Nature* 415 (6875), 1014.
- Chapman, J.S., Melbourne, T.L., 2009. Future Cascadia megathrust rupture delineated by episodic tremor and slip. *Geophys. Res. Lett.* 36 (22), 1–5.
- Chen, K., Smith, J.D., Avouac, J.-P., Liu, Z., Song, Y.T., Gualandri, A., 2019. Triggering of the Mw 7.2 Hawaii earthquake of May 4, 2018 by a dike intrusion. *Geophys. Res. Lett.*
- Clark, K., Howarth, J., Litchfield, N., Cochran, U., Turnbull, J., Dowling, L., et al., 2019. Geological evidence for past large earthquakes and tsunamis along the Hikurangi subduction margin, New Zealand. *Mar. Geol.* 412, 139–142.
- Delaney, P.T., Denlinger, R.P., Lisowski, M., Miklius, A., Okubo, P.G., Okamura, A.T., Sakoi, M.K., 1998. Volcanic spreading at Kilauea, 1976–1996. *J. Geophys. Res., Solid Earth* 103 (B8), 18003–18023.
- Denlinger, R.P., Okubo, P., 1995. Structure of the mobile south flank of Kilauea Volcano, Hawaii. *J. Geophys. Res., Solid Earth* 100 (B12), 24499–24507.
- Dieterich, J.H., 1978. Time-dependent friction and the mechanics of stick-slip. In: *Rock Friction and Earthquake Prediction*. Birkhäuser, Basel, pp. 790–806.
- Dieterich, J.H., 1979. Modeling of rock friction: 1. Experimental results and constitutive equations. *J. Geophys. Res., Solid Earth* 84 (B5), 2161–2168.
- Dixon, T.H., Jiang, Y., Malservisi, R., McCaffrey, R., Voss, N., Protti, M., Gonzalez, V., 2014. Earthquake and tsunami forecasts: relation of slow slip events to subsequent earthquake rupture. *Proc. Natl. Acad. Sci.* 111 (48), 17039–17044.
- Foster, J.H., Lowry, A.R., Brooks, B.A., 2013. Fault frictional parameters and material properties revealed by slow slip events at Kilauea volcano, Hawaii. *Geophys. Res. Lett.* 40 (23), 6059–6063.
- Frankel, A., Chen, R., Petersen, M., Moschetti, M., Sherrod, B., 2015. 2014 update of the Pacific Northwest portion of the US National Seismic Hazard Maps. *Earthq. Spectra* 31 (S1), S131–S148.
- Furumoto, A.S., Kovach, R.L., 1979. GL03309 I: P 9. *Phys. Earth Planet. Inter.* 18, 197–208.
- Galetzka, J., Melgar, D., Genrich, J.F., Geng, J., Owen, S., Lindsey, E.O., et al., 2015. Slip pulse and resonance of the Kathmandu basin during the 2015 Gorkha earthquake, Nepal. *Science* 349 (6252), 1091–1095.
- Gillard, D., Wyss, M., Okubo, P., 1996. Type of faulting and orientation of stress and strain as a function of space and time in Kilauea's south flank, Hawaii. *J. Geophys. Res., Solid Earth* 101 (B7), 16025–16042.
- Got, J.L., Okubo, P., 2003. New insights into Kilauea's volcano dynamics brought by large-scale relative relocation of microearthquakes. *J. Geophys. Res., Solid Earth* 108 (B7).
- Hawthorne, J.C., Rubin, A.M., 2013. Laterally propagating slow slip events in a rate and state friction model with a velocity-weakening to velocity-strengthening transition. *J. Geophys. Res., Solid Earth* 118 (7), 3785–3808.
- Hill, D.P., 1969. Crustal structure of the Island of Hawaii from seismic-refraction measurements. *Bull. Seismol. Soc. Am.* 59 (1), 101–130.
- Ito, Y., Hino, R., Kido, M., Fujimoto, H., Osada, Y., Inazu, D., et al., 2013. Episodic slow slip events in the Japan subduction zone before the 2011 Tohoku-Oki earthquake. *Tectonophysics* 600, 14–26.
- Klein, F.W., Koyanagi, R.Y., Nakata, J.S., Tanigawa, W.R., 1987. Volcanism in Hawaii. *U. S. Geol. Surv. Prof. Pap.* 1350, 1019–1185.
- Lay, T., Ye, L., Kanamori, H., Satake, K., 2018. Constraining the dip of shallow, shallowly dipping thrust events using long-period love wave radiation patterns: applications to the 25 October 2010 Mentawai, Indonesia, and 4 May 2018 Hawaii island earthquakes. *Geophys. Res. Lett.* 45 (19), 10–342.
- Liu, C., Lay, T., Xiong, X., 2018. Rupture in the 4 May 2018 Mw 6.9 earthquake seaward of the Kilauea east rift zone fissure eruption in Hawaii. *Geophys. Res. Lett.* 45 (18), 9508–9515.
- Liu, Y., Rice, J.R., 2009. Slow slip predictions based on granite and gabbro friction data compared to GPS measurements in northern Cascadia. *J. Geophys. Res., Solid Earth* 114 (B9).
- Melgar, D., Fan, W., Riquelme, S., Geng, J., Liang, C., Fuentes, M., et al., 2016. Slip segmentation and slow rupture to the trench during the 2015, Mw8.3 Illapel, Chile earthquake. *Geophys. Res. Lett.* 43 (3), 961–966.
- Montgomery-Brown, E.K., Segall, P., Miklius, A., 2009. Kilauea slow slip events: identification, source inversions, and relation to seismicity. *J. Geophys. Res., Solid Earth* 114 (B6).
- Morgan, J.K., Moore, G.F., Hills, D.J., Leslie, S., 2000. Overthrusting and sediment accretion along Kilauea's mobile south flank, Hawaii: evidence for volcanic spreading from marine seismic reflection data. *Geology* 28 (7), 667–670.
- Nakamura, Kazuaki, 1982. Why do long rift zones develop better in Hawaiian volcanoes: a possible role of thick oceanic sediments. *Arquipélago. Série Ciências da Natureza* 3, 59–73.
- Obara, K., 2002. Nonvolcanic deep tremor associated with subduction in southwest Japan. *Science* 296 (5573), 1679–1681.
- Owen, S., Bürgmann, R., 2006. An increment of volcano collapse: kinematics of the 1975 Kalapana, Hawaii, earthquake. *J. Volcanol. Geotherm. Res.* 150 (1–3), 163–185.
- Owen, S., Segall, P., Freymueller, J., Mikijus, A., Denlinger, R., Árnadóttir, T., et al., 1995. Rapid deformation of the south flank of Kilauea volcano, Hawaii. *Science* 267 (5202), 1328–1332.
- Park, J., Morgan, J., Zelt, C., Okubo, P., Peters, L., Benesh, N., 2007. Comparative velocity structure of active Hawaiian volcanoes from 3-d onshore-offshore seismic tomography. *Earth Planet. Sci. Lett.* 259 (3–4), 500–516.
- Radiguet, M., Perfettini, H., Cotte, N., Gualandri, A., Valette, B., Kostoglodov, V., et al., 2016. Triggering of the 2014 Mw 7.3 Papanoa earthquake by a slow slip event in Guerrero, Mexico. *Nat. Geosci.* 9 (11), 829.
- Ramos, M.D., Huang, Y., 2019. How the transition region along the Cascadia megathrust influences coseismic behavior: insights from 2-D dynamic rupture simulations. *Geophys. Res. Lett.* 46 (4), 1973–1983.
- Rogers, G., Dragert, H., 2003. Episodic tremor and slip on the Cascadia subduction zone: the chatter of silent slip. *Science* 300 (5627), 1942–1943.
- Rolandone, F., Nocquet, J.M., Mothes, P.A., Jarrin, P., Vallée, M., Cubas, N., et al., 2018. Areas prone to slow slip events impede earthquake rupture propagation and promote afterslip. *Sci. Adv.* 4 (1), eaao6596.
- Romano, F., Piatanesi, A., Lorito, S., Tolomei, C., Atzori, S., Murphy, S., 2016. Optimal time alignment of tide-gauge tsunami waveforms in nonlinear inversions: application to the 2015 Illapel (Chile) earthquake. *Geophys. Res. Lett.* 43 (21), 11–226.
- Rubin, A.M., 2008. Episodic slow slip events and rate-and-state friction. *J. Geophys. Res., Solid Earth* 113 (B11).
- Ruina, A., 1983. Slip instability and state variable friction laws. *J. Geophys. Res., Solid Earth* 88 (B12), 10359–10370.
- Saffer, D.M., Wallace, L.M., 2015. The frictional, hydrologic, metamorphic and thermal habitat of shallow slow earthquakes. *Nat. Geosci.* 8 (8), 594–600.
- Satake, K., Fujii, Y., Harada, T., Namegaya, Y., 2013. Time and space distribution of coseismic slip of the 2011 Tohoku earthquake as inferred from tsunami waveform data. *Bull. Seismol. Soc. Am.* 103 (2B), 1473–1492.
- Segall, P., Bradley, A.M., 2012. Slow-slip evolves into megathrust earthquakes in 2D numerical simulations. *Geophys. Res. Lett.* 39 (18).
- Segall, P., Desmarais, E.K., Shelly, D., Miklius, A., Cervelli, P., 2006. Earthquakes triggered by silent slip events on Kilauea volcano, Hawaii. *Nature* 442 (7098), 71.
- Segall, P., Rubin, A.M., Bradley, A.M., Rice, J.R., 2010. Dilatant strengthening as a mechanism for slow slip events. *J. Geophys. Res., Solid Earth* 115 (B12).
- Skarbek, R.M., Rempel, A.W., Schmidt, D.A., 2012. Geologic heterogeneity can produce aseismic slip transients. *Geophys. Res. Lett.* 39 (21).
- Thomas, A.M., Beroza, G.C., Shelly, D.R., 2016. Constraints on the source parameters of low-frequency earthquakes on the San Andreas Fault. *Geophys. Res. Lett.* 43 (4), 1464–1471.
- Thomas, A.M., Bürgmann, R., Shelly, D.R., Beeler, N.M., Rudolph, M.L., 2012. Tidal triggering of low frequency earthquakes near Parkfield, California: implications

- for fault mechanics within the brittle-ductile transition. *J. Geophys. Res., Solid Earth* 117 (B5).
- Thurber, C.H., Gripp, A.E., 1988. Flexure and seismicity beneath the south flank of Kilauea volcano and tectonic implications. *J. Geophys. Res., Solid Earth* 93 (B5), 4271–4278.
- Thurber, C.H., Li, Y., Johnson, C., 1989. Seismic detection of a low-velocity layer beneath the southeast flank of Mauna Loa, Hawaii. *Geophys. Res. Lett.* 16 (7), 649–652.
- Tsang, L.L., Meltzner, A.J., Philipposian, B., Hill, E.M., Freymueller, J.T., Sieh, K., 2015. A 15 year slow-slip event on the Sunda megathrust offshore Sumatra. *Geophys. Res. Lett.* 42 (16), 6630–6638.
- Wallace, L.M., Webb, S.C., Ito, Y., Mochizuki, K., Hino, R., Henrys, S., et al., 2016. Slow slip near the trench at the Hikurangi subduction zone, New Zealand. *Science* 352 (6286), 701–704.
- Yamashita, Y., Yakiwara, H., Asano, Y., Shimizu, H., Uchida, K., Hirano, S., Kamizono, M., 2015. Migrating tremor off southern Kyushu as evidence for slow slip of a shallow subduction interface. *Science* 348 (6235), 676–679.